

The role of Al₂O₃ interlayer in the synthesis of ZnS/Al₂O₃/MoS₂ core-shell nanowires

Edgars Butanovs^{1,3}, Alexei Kuzmin¹, Aleksejs Zolotarjovs¹, Sergei Vlassov², Boris Polyakov^{1}*

¹Institute of Solid State Physics, University of Latvia, Kengaraga street 8, LV-1063 Riga, Latvia

²Institute of Physics, University of Tartu, W. Ostwaldi Str. 1, 50412, Tartu, Estonia

³Institute of Technology, University of Tartu, Nooruse 1, 50411 Tartu, Estonia

*e-mail: boris.polyakov@cfi.lu.lv

Abstract

During the synthesis of heterostructured nanomaterials, unwanted structural and morphological changes in nanostructures may occur, especially when multiple sequential growth steps are involved. In this study, we describe a synthesis strategy of heterostructured ZnS/Al₂O₃/MoS₂ core-shell nanowires (NWs), and explore the role of the Al₂O₃ interlayer during synthesis. Core-shell NWs were produced via a four-step route: 1) synthesis of ZnO NWs on a silicon wafer, 2) deposition of thin Al₂O₃ layer by ALD, 3) magnetron deposition of MoO₃ layer, and 4) annealing of the sample in the sulphur atmosphere. During sulphurization, ZnO is converted into ZnS, and MoO₃ into MoS₂, while the Al₂O₃ interlayer preserves the smooth surface of an NW required for the growth of a continuous MoS₂ shell. The resulting ZnS/Al₂O₃/MoS₂ core-shell NWs were characterized by transmission electron microscopy, X-ray diffraction and photoelectron spectroscopy, Raman spectroscopy, and optical photoluminescence spectroscopy. A reported strategy can be used for the synthesis of other core-shell NWs with a transition metal dichalcogenides (TMDs) shell to protect the NW core material that may otherwise be altered or damaged by the reactive chalcogenides at high temperatures.

Keywords: Core-shell nanowires, transition metal dichalcogenides, ZnO, ZnS, Al₂O₃, MoS₂

1. Introduction

In recent years, two-dimensional (2D) transition metal dichalcogenides (TMDs) have become a topic of interest within the materials-research scientific community [1]. TMDs with the general formula MX_2 (e.g., $\text{M} = \text{W}, \text{Mo}$, etc., $\text{X} = \text{S}, \text{Se}, \text{Te}$) have an indirect bandgap in bulk form but transform to direct energy bandgap semiconductors when scaled down to a few atomic layers [2,3]. Molybdenum disulfide (MoS_2) is one of the most studied and well-known 2D TMDs materials [4], and can be synthesized in the form of powder, few-layer or monolayer 2D nanosheets, nanoflakes, and nanotubes [5]. MoS_2 is an n-type semiconductor; however, the origin of this unintentional doping is still not clear [6]. MoS_2 has the indirect $E_{\text{ig}} = 1.2$ eV and direct $E_{\text{dg}} = 1.8$ eV bandgap in bulk and monolayer forms, respectively, and is non-toxic and thermally and chemically stable [7]. Some of the physical properties of MoS_2 , including a direct bandgap in low-dimensional structures, strong interaction of light with matter, and good carrier mobility, have aroused interest in this material in the field of optoelectronics and photodetection [8]. On the other hand, MoS_2 exhibits excellent catalytic properties and good potential for photocatalytic production of solar fuels like hydrogen gas [9]. A number of studies are dedicated to the synthesis and characterization of hybrid nanostructures that incorporate layered MoS_2 . [10–15] In particular, MoS_2 is often combined with ZnO [10,14–19] and ZnS [10,20–22], governed by the attractive properties of these materials.

Bulk zinc oxide (ZnO) is a direct bandgap (3.4 eV) n-type semiconductor [23] and has two main phases: hexagonal wurtzite (P63mc) and cubic (Fm3m) zincblende. Nanostructured ZnO has been of interest to the scientific community for decades, and is still very popular due to the simplicity of its synthesis (no need to use expensive raw materials or complex equipment) and numerous morphological shapes and nanostructures (NWs, nanobelts, nanotubes, etc.), which make it very attractive as a nano-template material [24].

Zinc sulfide (ZnS) is a direct bandgap semiconductor with a bandgap of 3.6 eV for the most stable zincblende phase, and 3.9 eV for the high-temperature wurtzite phase [25]. ZnS is a

low-cost, environmentally friendly compound with attractive mechanical properties, such as good fracture strength and hardness. ZnS is transparent in a wide wavelength range and is widely used for electroluminescent applications and nanophosphors [26]. ZnS NWs have shown promise in electronics, optoelectronics, and sensor applications [27].

Core-shell nanowire-based architecture is highly promising for different solar energy harvesting applications [28,29]. ZnO/MoS₂ hybrid heterostructures are promising for photocatalytic reactions, including the hydrogen evolution reaction [10,14–19]. These [10,20–22] nanostructures are also shown to possess favorable optical properties, including enhanced photoelectric performance [30], making them potentially suitable for imaging and sensing applications. In addition, we recently demonstrated that it is possible to combine all three materials and their useful properties into a single ZnO/ZnS/MoS₂ core-shell heterostructure [10]; however, we found that during high-temperature synthesis of ZnS/MoS₂ core-shell NWs, ZnO is partially or completely converted into ZnS, which causes severe morphological changes in the NW core [10].

Al₂O₃ is an environmentally-friendly and technologically important material with high hardness and chemical stability [31], and can exist in many crystallographic modifications possessing different properties. The reported experimental band gap value is 8.8 eV for α -Al₂O₃, 7.0–8.7 eV for γ -Al₂O₃, and 5.1–7.1 eV for amorphous Al₂O₃ [32]. A thin layer of amorphous Al₂O₃ can be deposited with high uniformity and thickness accuracy using the atomic layer deposition (ALD) technique at low temperatures [33]. Furthermore, it has been shown that a thin Al₂O₃ layer can be used for the chemical and mechanical protection of metallic nanowires (NWs) [34].

In this study, we report on the synthesis of ZnS/Al₂O₃/MoS₂ core-shell NWs and demonstrate the protective role of the Al₂O₃ interlayer during the chemical conversion of ZnO and MoO₃ into ZnS and MoS₂, respectively, during annealing in the sulphur atmosphere. The choice of the Al₂O₃ interlayer can be explained by three main factors: 1) Al₂O₃ material has high

chemical stability in the sulphur environment at elevated temperatures; 2) the ALD deposition process of Al_2O_3 is a well-established technological process, which allows controlling shell thickness with sub-nanometer precision; and 3) MoS_2 and other TMDs materials were successfully grown on both crystalline and amorphous Al_2O_3 substrates. ZnO NWs are convenient 1D templates for core-shell synthesis of nanomaterials. A combination of ZnO NWs with an Al_2O_3 interlayer may be useful for many other TMDs materials synthesis, where the sacrificial precursor layer is selenized or sulphurized at elevated temperatures.

2. Experimental details.

$\text{ZnS}/\text{Al}_2\text{O}_3/\text{MoS}_2$ core-shell NWs were produced via a four-step route: 1) synthesis of ZnO NWs on a silicon wafer; 2) deposition of thin Al_2O_3 layer by ALD; 3) magnetron deposition of the MoO_3 layer; and 4) annealing of the sample in the sulphur atmosphere.

ZnO NWs were grown by a chemical vapor transport method using spherical Au nanoparticles as a catalyst (50 nm in diameter, water suspension, *BBI International*) [7]. A 1:4 mixture of ZnO and graphite powders was heated to 900 °C in a quartz tube for 30 minutes in a stream of the carrier N_2 gas. NWs were synthesized on top of the oxidized silicon wafers Si/SiO_2 (Si (100) wafer, 50 nm of thermal oxide, *Semiconductor Wafer, Inc.*). Al_2O_3 films were grown in the ALD reactor Savannah S100. The films were grown at 150 °C by applying 66 cycles of Trimethylaluminum (TMA) and H_2O as precursors, and inert gas (N_2) flow. Next, $\text{ZnO}/\text{Al}_2\text{O}_3$ NW samples were coated with a layer of amorphous a-MoO_3 , having a 30 nm thickness on a flat substrate, and using reactive dc magnetron sputtering of metallic tungsten target in a mixed Ar/O_2 atmosphere. Finally, the samples were annealed in a quartz tube in a sulphur atmosphere using N_2 as a carrier gas for 30 minutes at 750 °C to convert the molybdenum precursor (MoO_3) into MoS_2 .

2D microcrystals of MoS_2 used as the reference sample for micro-Raman measurements were grown for 20 minutes on a Si/SiO_2 substrate in a quartz tube using 1 mg MoO_3 (99.5%,

Sigma Aldrich) and 0.25 g sulfur (99.98%, *Sigma Aldrich*) powders as precursor materials and N₂ as a carrier gas. Silicon substrate was placed downstream of precursors in the high-temperature zone (700 °C).

ZnS NWs were synthesized as reference material for XRD and PL measurements. NWs were synthesized on top of the oxidized silicon wafers Si/SiO₂ using the same Au nanoparticles as a catalyst. ZnS powder 0.4 g (> 97%, *Sigma Aldrich*) was thermally sublimated in a quartz tube at a temperature of 950 °C for 30 minutes, followed by natural cooling. The ZnS vapor was carried downstream by N₂ gas to the substrate to grow ZnS NWs.

The phase composition of the samples was studied with X-ray diffraction (XRD) using a Rigaku MiniFlex 600 X-ray powder diffractometer, Bragg-Brentano θ -2 θ geometry, and a 600 W Cu anode (Cu K α radiation, $\lambda = 1.5406 \text{ \AA}$) X-ray tube. The inner crystalline structure of core-shell NWs transferred on the Lacey Cu TEM grid (*Agar Scientific*) was revealed using TEM (Tecnai GF20, FEI) operated at the accelerating voltage of 200 kV.

X-ray photoelectron spectroscopy (XPS) measurements were performed using an ESCALAB Xi (ThermoFisher) X-ray photoelectron spectrometer. The spectra were calibrated relative to the adventitious C 1s peak at 284.8 eV.

Micro-Raman spectra were measured using a TriVista 777 confocal Raman system (Princeton Instruments/Acton, 750 mm focal length, 600 lines/mm grating) equipped with an upright Olympus microscope with an Olympus UIS2 LMPlanFLN 20x/0.40 objective. The Raman spectra were excited by a continuous-wave, single-frequency, diode-pumped laser Cobolt Samba 150 ($\lambda = 532 \text{ nm}$) and recorded with an Andor iDus DV420A-OE CCD camera. The laser power on the sample was controlled by a set of neutral density filters and was set to about 2.1 mW.

Imaging experiments were performed at room temperature using a confocal microscope with spectrometer Nanofinder-S (SOLAR TII) [35,36]. The confocal reflection and spectral images were recorded in a back-scattering geometry with a Nikon CF Plan Apo 100 \times (NA=0.95)

optical objective in a raster-scanning mode. A diode-pumped solid-state (DPSS) Nd: YAG laser (532 nm, max continuous wave (cw) power $P_{ex}=150$ mW) was used as the photoluminescence (PL) excitation source. The PL signal was dispersed by 150 grooves/mm diffraction grating mounted in the 520 mm focal length monochromator, and two Hamamatsu R928 photomultiplier tubes were used as detectors. To avoid sample damage, the laser power at the sample was controlled by a variable neutral filter.

Room-temperature photoluminescence (PL, Hamamatsu R92P PMT) spectra with a 266 nm excitation wavelength (fourth harmonic of CryLas Nd:YAG laser, 0.3 mJ power, 1 ns pulse duration, 5 kHz repetition rate) were measured to investigate the as-prepared nanostructure optical properties.

The thickness of MoS₂ 2D microcrystals was measured with an atomic force microscope (AFM, CP-II, Veeco) in the tapping mode using PPP-NCHR probes with a force constant of 42 N/m and tip radius of curvature < 10 nm (Nanosensors).

3. Results and discussion.

The phase composition of NWs grown on oxidized Si substrates and annealed in the air at 750 °C (ZnO/Al₂O₃) after sulphurisation (ZnS/MoS₂ and ZnS/Al₂O₃/MoS₂) was studied using the XRD method (Fig. 1). According to XRD data, no ZnO phase was present in NWs after sulphurisation, meaning ZnO was completely converted to the ZnS phase. Such behavior was expected since sulphur reacts with ZnO (ICDD 36-1451) at temperatures above 400 °C, resulting in the formation of the ZnS phase (ICDD 36-1450) [37]. No Bragg peaks of the MoO₃ phase were found in NWs covered with a molybdenum oxide shell, but the (002) MoS₂ peak (ICDD 37-1492) was detected, indicating the full conversion of MoO₃ into MoS₂ during sulphurisation. Also, no peaks of Al₂O₃ were observed, likely due to the small thickness of the Al₂O₃ shell. Several other Bragg peaks present on XRD patterns were attributed to the Si(100) substrate

(forbidden Si(200) reflection at $2\theta \approx 33^\circ$), cristobalite SiO_2 (ICDD 36-1451), and the gold nanoparticles used for VLS growth (ICDD 04-0784).

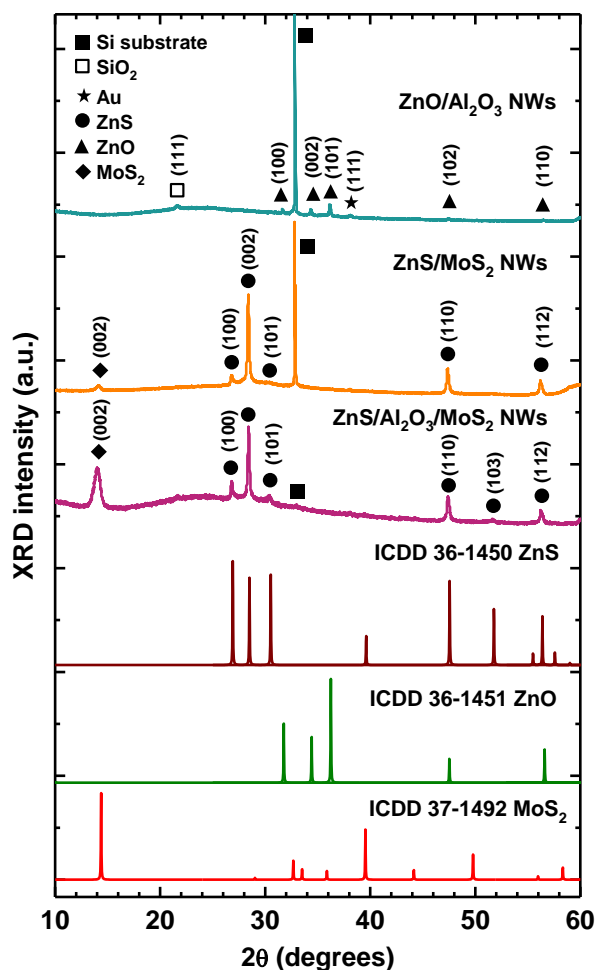


Figure 1. XRD patterns of NWs annealed in the air ($\text{ZnO}/\text{Al}_2\text{O}_3$) and after sulphurisation (ZnS/MoS_2 and $\text{ZnS}/\text{Al}_2\text{O}_3/\text{MoS}_2$).

In addition to XRD measurements, XPS analysis was performed on the as-prepared NWs to verify the elemental composition and study the chemical states of the component ions in the nanostructures. XPS spectra for the ZnS/MoS_2 and $\text{ZnS}/\text{Al}_2\text{O}_3/\text{MoS}_2$ NWs are shown in Fig. 2., while the spectra of the reference samples (ZnO , ZnO-ZnS , ZnS , $\text{ZnO-Al}_2\text{O}_3$, and $\text{ZnO-Al}_2\text{O}_3\text{-MoO}_3$ NWs), which were used to determine peak relative shifts and perform detailed chemical-state analysis of the various compounds, are provided in the Supplementary Information in Fig.S1.

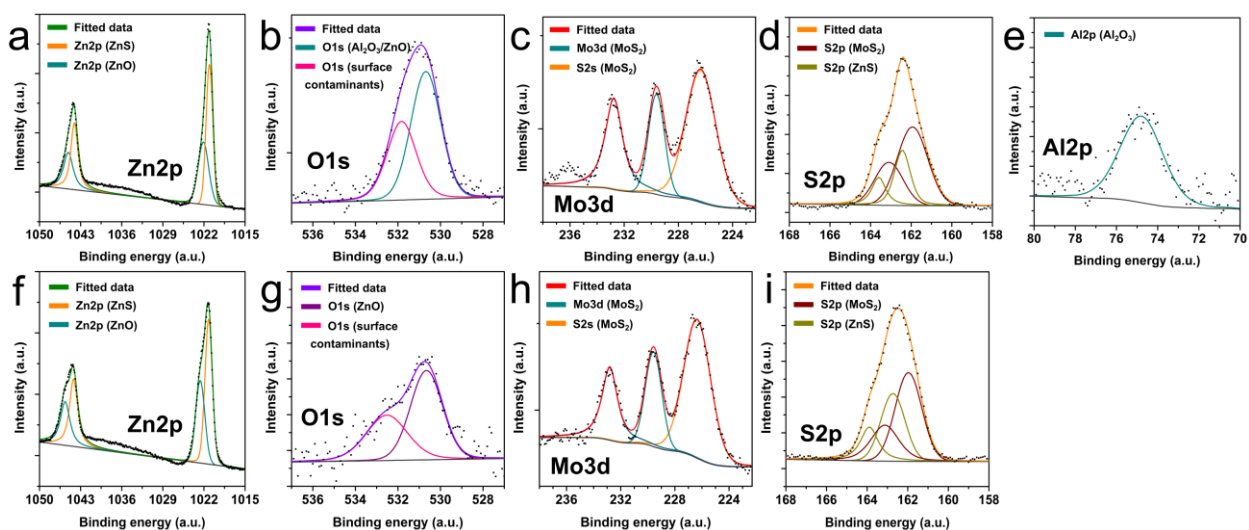


Figure 2. High-resolution XPS spectra and peak fits for elements in the sulphurized NWs (a-e) ZnS/Al₂O₃/MoS₂ and (f-i) ZnS/MoS₂ NWs.

The composition analysis confirmed the presence of the expected elements in the samples and did not show any impurities. The high-resolution scans of each element's characteristic peaks provided information on the chemical states. Zinc Zn 2p scans (see Fig. 2(a,f)) gave qualitatively similar results for both samples: a pair of Zn 2p_{3/2} (at 1021.2 eV binding energy) and 2p_{1/2} peaks with spin-orbit splitting $\Delta_{3/2-1/2}=23$ eV was attributed to ZnS compound, and a pair of significantly weaker peaks shifted slightly to a higher energy (Zn 2p_{3/2} at 1022.1 eV) was attributed to ZnO, thus showing a remaining amount of the compound in the NWs, which XRD measurements did not detect. The shift between the Zn compounds was also observed in the ZnO, ZnO-ZnS, and ZnS reference samples (see Fig.S1(a,c,e)) as was previously reported in the literature [38,39]. Oxygen O 1s scans Fig.2(b,g) show the typical metal oxide peak centered at around 530.4 eV with a broader shoulder at 532-533 eV attributed to organic contaminants on the surface (C-O and C=O bonds). Both Al₂O₃ and ZnO compounds contribute to the peak in the ZnS/Al₂O₃/MoS₂ sample, while weak ZnO contribution was observed in the ZnS/MoS₂ sample. Molybdenum Mo 3d scans (Fig.2(c,h)) revealed three peaks: two Mo 3d 5/2 (at 229.6 eV) and 3/2 peaks with 3.2 eV spin-orbit splitting assigned to the MoS₂ compound, as well as an overlapping S 2s peak at 226.2 eV. An Mo 3d_{5/2} peak at 233 eV (see Fig.S1(k)) for MoO₃ was not observed, thus confirming that the precursor MoO₃ coating was fully converted. Sulphur S

2p scans in Fig.2(d,i) show a broad peak around 162.3 eV, which consists of contributions from pairs of S 2p 3/2 and 1/2 ($\Delta_{3/2-1/2}=1.16$ eV) for both MoS₂ and ZnS compounds. The Zn peaks for ZnS are shifted slightly to a higher energy compared to the peaks for MoS₂, as has been reported before [40]. Finally, Al 2p peak (see Fig.2(e)) at 74.8 eV is typically associated with the Al₂O₃ compound. The XPS measurements clearly show that the introduction of the Al₂O₃ interlayer does not affect the chemistry of the desired compounds in the heterostructures, as the XPS results for the samples with and without Al₂O₃ have qualitatively similar results.

Raman spectroscopy was used to fingerprint the presence of the MoS₂ phase. The obtained Raman spectra of the core-shell NWs (Fig. 3) confirm the formation of the MoS₂ layer around the ZnS NW core.

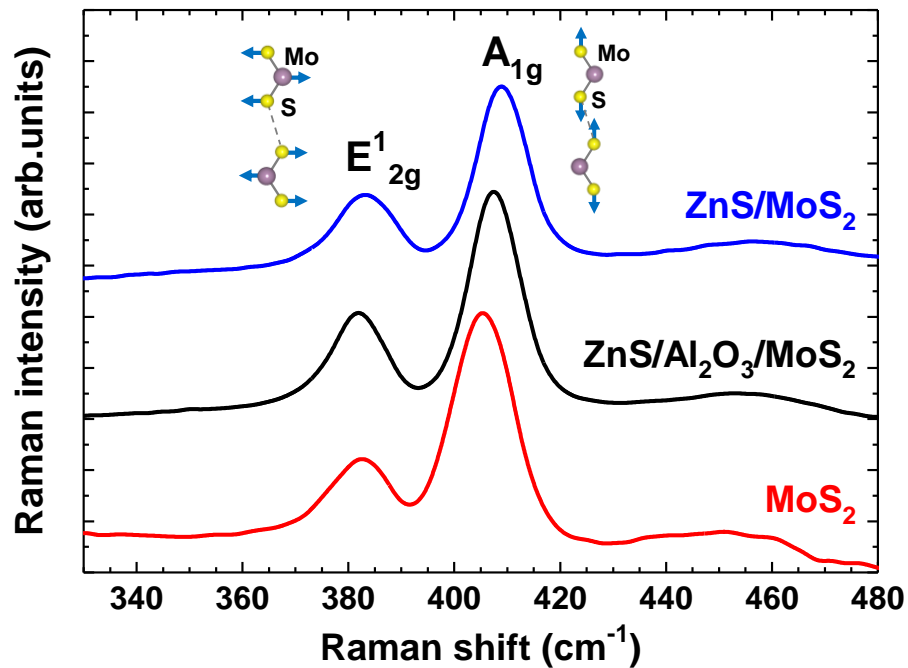


Figure 3. Typical Raman spectra of ZnS/MoS₂ and ZnS/Al₂O₃/MoS₂ NWs and pure MoS₂.

Two first-order Raman active modes (in-plane E_{2g}^1 and out-of-plane A_{1g}) are indicated.

Two Raman-active zone center phonon modes, the in-plane E_{2g}^1 mode at 384 cm⁻¹ and the out-of-plane A_{1g} mode at 407 cm⁻¹, are well resolved [41–44]. Raman bands due to ZnO [45], ZnS [46], and Al₂O₃ [47] phases were not observed. Note that the Raman spectrum of the ZnS/MoS₂ sample has a strong background of increasing towards a large Raman shift, i.e., long wavelength

(not visible in the range shown in Fig. 3). The origin of this contribution is the photoluminescence from the direct excitonic transitions in a few-layer MoS₂ [2]. The absence of photoluminescence in the samples with the Al₂O₃ interlayer suggests that the presence of Al₂O₃ stimulates the growth of MoS₂ multilayers.

TEM microscopy was used to gain a deeper insight into the inner structure of core-shell NWs (Fig.4). As was reported in our previous work, sulfurization of ZnO/MoO₃ NWs at 700° C and conversion of ZnO into ZnS cause morphological changes [10]. With the increase in temperature up to 750°C, morphological changes in core-shell NW structures become more expressed (Fig. 4a-c). According to XRD data, after sulfurization, ZnO/MoO₃ NW converts into ZnS/MoS₂, and MoS₂ microcrystals can be distinguished at high magnification (Fig. 4c). As previously mentioned, a thin layer of amorphous Al₂O₃ was deposited by ALD as a protective shell around ZnO NWs. TEM images of ZnO/Al₂O₃ core-shell NW annealed in air at 750°C are shown in Fig. 4d-f at different magnifications. Complete crystallization of the Al₂O₃ shell occurs during NW annealing (Fig. 4c). According to the analysis of the SAED data, the Al₂O₃ layer grows in conformity to the m-plane of ZnO (Supplementary materials, Fig. S2). Due to absence of Al₂O₃ contribution in the XRD patterns, it is difficult to identify the crystalline phase of the Al₂O₃ shell (Supplementary materials, Fig. S3-4). According to the literature, ALD-deposited amorphous Al₂O₃ films can be crystallized in the alpha or gamma phase [48]. The possibility of epitaxial growth of m-plane ZnO on a (10-10) plane of α -Al₂O₃ was reported by Ku et al. [49]. A sulfurized ZnS/Al₂O₃/MoS₂ core-shell NW is shown in Fig. 4g-i. The layers of MoS₂ grown from MoO₃ upon sulphurisation on the NW surface are distinguishable as parallel black lines. Typically, the thickness of the coating varies between 5 and 10 monolayers, with interlayer distance measured around 6.25 Å, which corresponds with the 6.2–6.3 Å interlayer distance in MoS₂ nanostructures [16,50]. We conclude that the Al₂O₃ interlayer was able to preserve the straight shape of the ZnO NW and facilitate the growth of MoS₂ parallel to the NW surface.

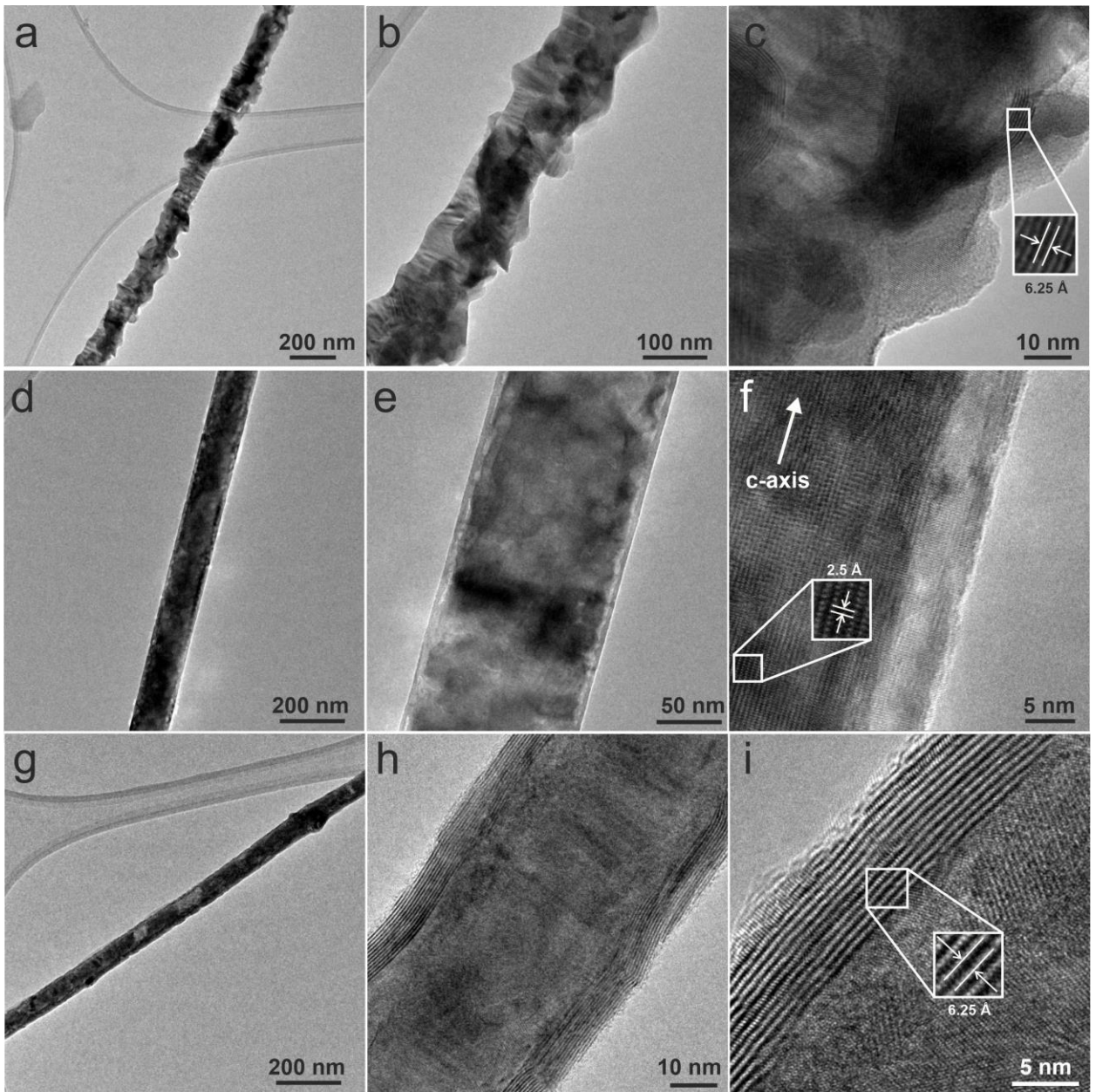


Figure 4. TEM images of ZnS/MoS_2 (a-c), $\text{ZnO}/\text{Al}_2\text{O}_3$ (d-f), and $\text{ZnS}/\text{Al}_2\text{O}_3/\text{MoS}_2$ (g-i) NWs annealed at 750°C .

It is an open question whether amorphous or crystalline Al_2O_3 is needed for the growth of qualitative MoS_2 . According to Peters et al., MoS_2 2D crystals can be grown on c-plane, r-plane, a-plane, and m- planes of $\alpha\text{-Al}_2\text{O}_3$ substrates, but aligned growth occurs only on the r- and m-plane sapphire [51]. In the work of Ma et al., aligned rectangle-shaped MoS_2 2D crystals were grown on the a-plane of sapphire [52], and high-quality MoS_2 2D crystals were grown by CVD on an amorphous Al_2O_3 substrate by Bergeron et al. [53]. The crystallization temperature of α -

MoO₃ is about 340 °C [54], while the crystallization of amorphous Al₂O₃ was reported at temperatures above 650°C [55]. It is known that sulphuration of MoO₃ and conversion to MoS₂ begins at 500°C [10], meaning the MoS₂ layer likely starts to grow on the surface of the amorphous Al₂O₃ surface, and the main role of the Al₂O₃ interlayer is preserving the NW's straight shape.

Photoluminescence (PL) spectra of as-synthesized ZnS NWs, ZnS/MoS₂, and ZnS/Al₂O₃/MoS₂ NWs samples (ZnO/MoO₃ and ZnO/Al₂O₃/MoO₃ sulphurated at 750°C) measured at room temperature are shown in Fig. 5. The PL spectrum of ZnS NWs has a defect-related band at ~523 nm (2.37 eV) in good agreement with the literature [56,57]. For example, Chen et. al [57] attributes the PL band centered at 525 nm in the ZnS nanostructures to the Zn vacancies. Similarly, Wang et al. [56] attributed the peak at 2.40 eV (517 nm) to the presence of intrinsic vacancies such as the “S” vacancy acting as a donor center and the “Zn” vacancy acting as an acceptor. Up to 4 bands were observed in the experimental PL spectra of core-shell NWs and are described by Gaussian functions (shown as dotted lines in Fig. 5a). The PL spectrum of the ZnS/Al₂O₃/MoS₂ NWs contains both defect-related ZnS luminescence at ~520 nm (2.38 eV) and two luminescence bands related to direct excitonic transitions in MoS₂ at ~654 nm (1.90 eV) and ~707 nm (1.75 eV) [2]. An additional band at 580 nm (2.14 eV) can be seen in the PL spectrum of ZnS/MoS₂ NWs, which also appears as a “shoulder” in the ZnS/Al₂O₃/MoS₂ spectrum, the origin of which cannot be definitively identified. This band is related to sulfurized ZnO/Al₂O₃ NWs: a PL band in close wavelength spectral region ~616 nm (2.01 eV) can be seen for the ZnO/Al₂O₃ NWs sample sulfurized at 750° C (Fig. S6, Supplementary materials). On the other hand, ZnO crystals and ZnO nanomaterials have defect-related PL in the region of 2.2 eV [58]. It is possible that some amount of ZnO nanowires was not sulfurized completely to ZnS and gives a contribution to the PL spectra (note that XRD patterns did not contain any ZnO signal after sulfurization). In the PL spectrum of the ZnS/MoS₂ NWs, the band due to defect-related ZnS luminescence is reduced significantly, while MoS₂ related luminescence is similar to

that in ZnS/Al₂O₃/MoS₂ NWs. Splendiani et al. observed the photoluminescence peaks for the MoS₂ monolayer at 1.98 eV (626 nm) and 1.83 eV (678 nm), corresponding to the direct excitonic transitions with the energy split from valence band spin-orbital coupling. Note that this photoluminescence is observed only for monolayers or a few layers of MoS₂, and is absent in the indirect bandgap bulk MoS₂ sample. Confocal microscope images of MoS₂ 2D crystals grown on the Si/SiO₂ wafer are shown in Fig. 5b,c. The image in Fig. 5b was taken in the reflection mode for 532 nm, and the intensity of the gray color is proportional to the sample reflectivity, therefore, thicker regions of MoS₂ appear darker. The light color of the regions surrounding MoS₂ 2D crystals is due to the reflectivity of the Si substrate, whereas the bright regions at the center of the two MoS₂ 2D crystals are due to the high reflectivity of thick metallic-like MoS₂. The image in Fig. 5c is a photoluminescence map that was taken simultaneously with the reflectivity image in Fig. 5b. The PL was excited by a 532 nm laser line and measured at 685 nm, and the PL map correlates well with the reflectivity image. According to AFM measurements (Supplementary, Fig. S5), 2D MoS₂ crystals are thicker in the center (up to 250 nm) and thinner at the periphery (2-3 nm). There is no PL signal in the central region of 2D MoS₂ crystals (Fig. 5c) due to a transition from direct to indirect bandgap at higher thickness.

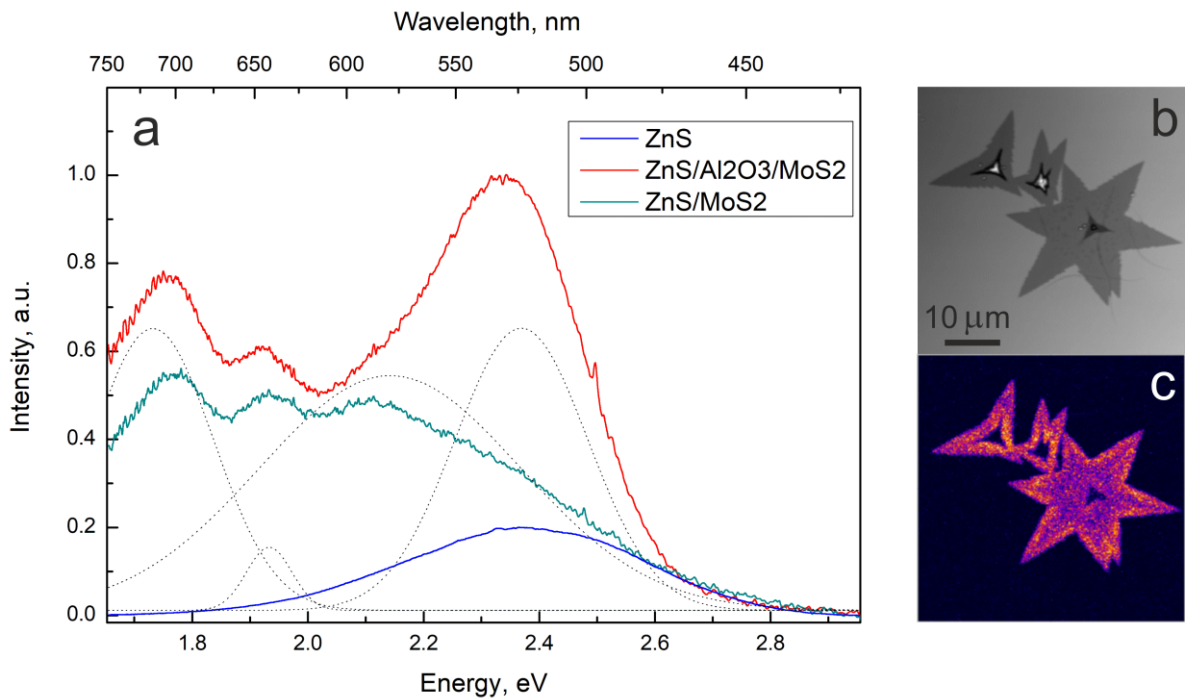


Figure 5. Room-temperature photoluminescence (PL) spectra at 266 nm excitation wavelength for the as-synthesized ZnS NWs, as well as ZnS/MoS₂ and ZnS/Al₂O₃/MoS₂ (ZnO/MoO₃ and ZnO/Al₂O₃/MoO₃ annealed in the sulphur atmosphere at 750°C) NWs (a). The PL spectrum of ZnS/Al₂O₃/MoS₂ NWs as a function of energy was decomposed on the energy scale into a set of Gaussian functions (dotted lines) to show separate contributions. The PL intensity is depicted in arbitrary units and does not contain information about relative intensities between the measured spectra. Confocal microscope images of MoS₂ microcrystals on Si/SiO₂ wafer: reflection mode image (b) and photoluminescence image excited by 532 nm laser line and measured at 685 nm (c). Artificial colors in (b, c) encode signal intensity: bright color corresponds to high PL intensity.

4. Conclusions.

In this study, the influence of the Al₂O₃ interlayer on the morphology of core-shell ZnS/Al₂O₃/MoS₂ NWs was explored. The synthesis of NWs involved the successive coating of ZnO NW templates by thin layers of Al₂O₃ and MoO₃ precursors, followed by annealing in a sulphur atmosphere at 750 °C. The sulphurisation process resulted in the growth of the MoS₂ shell and a conversion of the ZnO NW core into the ZnS phase, which causes unwanted morphology perturbation of NWs in the absence of the Al₂O₃ interlayer. We found that the introduction of the Al₂O₃ interlayer prevents morphological changes in the ZnO core during conversion to ZnS, thus preserving the NW's straight shape. The role of the amorphous Al₂O₃ interlayer is to separate and prevent the interactions between the ZnO core and the MoO₃ shell during the sulphurization process. The formation of a thin crystalline MoS₂ shell was confirmed by XRD, XPS, TEM, Raman, and optical photoluminescence spectroscopies.

Our approach, based on the use of the Al₂O₃ protective interlayer, can be applied for the synthesis of other core-shell NWs with a TMD shell, where the core material (e.g. ZnO NWs) can be altered by the reactive chalcogenides (S or Se) at high temperatures.

Acknowledgments

Financial support was provided by Latvian Science Council grant Nr. lzp-2020/1-0261. E.B. and S.V. were supported by the European Union's Horizon 2020 program, under Grant Agreement No. 856705 (ERA Chair "MATTER"). The authors are grateful to Armands Ozols for assistance in the synthesis of nanomaterials. The Institute of Solid State Physics, University of Latvia (Latvia) as the Centre of Excellence has received funding from the European Union's Horizon 2020 Framework Programme H2020-WIDESPREAD01-2016-2017-Teaming Phase2 under grant agreement no. 739508, project CAMART2.

References

- [1] W. Choi, N. Choudhary, G.H. Han, J. Park, D. Akinwande, Y.H. Lee, Recent development of two-dimensional transition metal dichalcogenides and their applications, *Mater. Today*. 20 (2017) 116–130. <https://doi.org/10.1016/j.mattod.2016.10.002>.
- [2] A. Splendiani, L. Sun, Y. Zhang, T. Li, J. Kim, C.-Y. Chim, G. Galli, F. Wang, Emerging Photoluminescence in Monolayer MoS₂, *Nano Lett.* 10 (2010) 1271–1275. <https://doi.org/10.1021/nl903868w>.
- [3] G.L. Frey, R. Tenne, M.J. Matthews, M.S. Dresselhaus, G. Dresselhaus, Optical Properties of MS₂ (M = Mo, W) Inorganic Fullerenelike and Nanotube Material Optical Absorption and Resonance Raman Measurements, *J. Mater. Res.* 13 (1998) 2412–2417. <https://doi.org/10.1557/JMR.1998.0335>.
- [4] U. Krishnan, M. Kaur, K. Singh, M. Kumar, A. Kumar, A synoptic review of MoS₂: Synthesis to applications, *Superlattices Microstruct.* 128 (2019) 274–297. <https://doi.org/10.1016/j.spmi.2019.02.005>.
- [5] I. Song, C. Park, H.C. Choi, Synthesis and properties of molybdenum disulphide: from bulk to atomic layers, *RSC Adv.* 5 (2015) 7495–7514. <https://doi.org/10.1039/C4RA11852A>.
- [6] K. Dolui, I. Rungger, S. Sanvito, Origin of the n -type and p -type conductivity of MoS₂ monolayers on a SiO₂ substrate, *Phys. Rev. B.* 87 (2013) 165402. <https://doi.org/10.1103/PhysRevB.87.165402>.
- [7] N. Wang, F. Wei, Y. Qi, H. Li, X. Lu, G. Zhao, Q. Xu, Synthesis of Strongly Fluorescent Molybdenum Disulfide Nanosheets for Cell-Targeted Labeling, *ACS Appl. Mater. Interfaces.* 6 (2014) 19888–19894. <https://doi.org/10.1021/am505305g>.
- [8] A. Taffelli, S. Dirè, A. Quaranta, L. Panzeri, MoS₂ Based Photodetectors: A Review, *Sensors.* 21 (2021) 2758. <https://doi.org/10.3390/s21082758>.
- [9] E. Parzinger, B. Miller, B. Blaschke, J.A. Garrido, J.W. Ager, A. Holleitner, U. Wurstbauer, Photocatalytic Stability of Single- and Few-Layer MoS₂, *ACS Nano.* 9 (2015) 11302–11309. <https://doi.org/10.1021/acs.nano.5b04979>.
- [10] E. Butanovs, A. Kuzmin, J. Butikova, S. Vlassov, B. Polyakov, Synthesis and characterization of ZnO/ZnS/MoS₂ core-shell nanowires, *J. Cryst. Growth.* 459 (2017) 100–104. <https://doi.org/10.1016/j.jcrysgro.2016.11.106>.
- [11] Z. Chen, D. Cummins, B.N. Reinecke, E. Clark, M.K. Sunkara, T.F. Jaramillo, Core-shell MoO₃-MoS₂ Nanowires for Hydrogen Evolution: A Functional Design for Electrocatalytic Materials, *Nano Lett.* 11 (2011) 4168–4175. <https://doi.org/10.1021/nl2020476>.

- [12] B. Han, S. Liu, N. Zhang, Y.-J. Xu, Z.-R. Tang, One-dimensional CdS@MoS₂ core-shell nanowires for boosted photocatalytic hydrogen evolution under visible light, *Appl. Catal. B Environ.* 202 (2017) 298–304. <https://doi.org/10.1016/j.apcatb.2016.09.023>.
- [13] F. Chen, T. Wang, L. Wang, X. Ji, Q. Zhang, Improved light emission of MoS₂ monolayers by constructing AlN/MoS₂ core-shell nanowires, *J. Mater. Chem. C* 5 (2017) 10225–10230. <https://doi.org/10.1039/C7TC03231E>.
- [14] S. Kumar, V. Sharma, K. Bhattacharyya, V. Krishnan, N-doped ZnO–MoS₂ binary heterojunctions: the dual role of 2D MoS₂ in the enhancement of photostability and photocatalytic activity under visible light irradiation for tetracycline degradation, *Mater. Chem. Front.* 1 (2017) 1093–1106. <https://doi.org/10.1039/C6QM00274A>.
- [15] M.-A. Kang, S. Kim, I.-S. Jeon, Y.R. Lim, C.-Y. Park, W. Song, S.S. Lee, J. Lim, K.-S. An, S. Myung, Highly efficient and flexible photodetector based on MoS₂–ZnO heterostructures, *RSC Adv.* 9 (2019) 19707–19711. <https://doi.org/10.1039/C9RA00578A>.
- [16] Y.-H. Tan, K. Yu, J.-Z. Li, H. Fu, Z.-Q. Zhu, MoS₂@ZnO nano-heterojunctions with enhanced photocatalysis and field emission properties, *J. Appl. Phys.* 116 (2014) 064305. <https://doi.org/10.1063/1.4893020>.
- [17] Y.-P. Lin, B. Polyakov, E. Butanovs, A.A. Popov, M. Sokolov, D. Bocharov, S. Piskunov, Excited States Calculations of MoS₂@ZnO and WS₂@ZnO Two-Dimensional Nanocomposites for Water-Splitting Applications, *Energies*. 15 (2022) 150. <https://doi.org/10.3390/en15010150>.
- [18] Y.-J. Yuan, F. Wang, B. Hu, H.-W. Lu, Z.-T. Yu, Z.-G. Zou, Significant enhancement in photocatalytic hydrogen evolution from water using a MoS₂ nanosheet-coated ZnO heterostructure photocatalyst, *Dalton Trans.* 44 (2015) 10997–11003. <https://doi.org/10.1039/C5DT00906E>.
- [19] Y. Liu, S. Xie, H. Li, X. Wang, A Highly Efficient Sunlight Driven ZnO Nanosheet Photocatalyst: Synergetic Effect of P-Doping and MoS₂ Atomic Layer Loading, *ChemCatChem*. 6 (2014) 2522–2526. <https://doi.org/10.1002/cctc.201402191>.
- [20] S. Harish, Prachi, J. Archana, M. Navaneethan, M. Shimomura, H. Ikeda, Y. Hayakawa, Synergistic interaction of 2D layered MoS₂/ZnS nanocomposite for highly efficient photocatalytic activity under visible light irradiation, *Appl. Surf. Sci.* 488 (2019) 36–45. <https://doi.org/10.1016/j.apsusc.2019.05.027>.
- [21] R. Gusain, N. Kumar, F. Opoku, P.P. Govender, S. Sinha, MoS₂ Nanosheet/ZnS Composites for the Visible-Light-Assisted Photocatalytic Degradation of Oxytetracycline, (n.d.) 12.
- [22] R.M. Clark, B.J. Carey, T. Daeneke, P. Atkin, M. Bhaskaran, K. Latham, I.S. Cole, K. Kalantar-zadeh, Two-step synthesis of luminescent MoS₂–ZnS hybrid quantum dots, *Nanoscale*. 7 (2015) 16763–16772. <https://doi.org/10.1039/C5NR04790K>.
- [23] Ü. Özgür, Ya.I. Alivov, C. Liu, A. Teke, M.A. Reshchikov, S. Doğan, V. Avrutin, S.-J. Cho, H. Morkoç, A comprehensive review of ZnO materials and devices, *J. Appl. Phys.* 98 (2005) 041301. <https://doi.org/10.1063/1.1992666>.
- [24] H. Liu, Z. Feng, J. Wang, J. Diao, D. Su, Synthesis of hollow carbon nanostructures using a ZnO template method, *New Carbon Mater.* 31 (2016) 87–91. [https://doi.org/10.1016/S1872-5805\(16\)60006-9](https://doi.org/10.1016/S1872-5805(16)60006-9).
- [25] H.C. Ong, R.P.H. Chang, Optical constants of wurtzite ZnS thin films determined by spectroscopic ellipsometry, *Appl. Phys. Lett.* 79 (2001) 3612–3614. <https://doi.org/10.1063/1.1419229>.
- [26] V. Dimitrova, J. Tate, Synthesis and characterization of some ZnS-based thin @lm phosphors for electroluminescent device applications, *Thin Solid Films.* (2000) 5.
- [27] X. Fang, T. Zhai, U.K. Gautam, L. Li, L. Wu, Y. Bando, D. Golberg, ZnS nanostructures: From synthesis to applications, *Prog. Mater. Sci.* 56 (2011) 175–287. <https://doi.org/10.1016/j.pmatsci.2010.10.001>.

- [28] B. Weng, S. Liu, Z.-R. Tang, Y.-J. Xu, One-dimensional nanostructure based materials for versatile photocatalytic applications, *RSC Adv.* 4 (2014) 12685. <https://doi.org/10.1039/c3ra47910b>.
- [29] S. Liu, Z.-R. Tang, Y. Sun, J.C. Colmenares, Y.-J. Xu, One-dimension-based spatially ordered architectures for solar energy conversion, *Chem. Soc. Rev.* 44 (2015) 5053–5075. <https://doi.org/10.1039/C4CS00408F>.
- [30] A. Aldalbahi, Z.-B. Wang, T. Ahamad, S.M. Alshehri, P.X. Feng, Two-Step Facile Preparation of 2D MoS₂/ZnO Nanocomposite - Junctions with Enhanced Photoelectric Performance, *Int. J. Photoenergy.* 2021 (2021) e1884293. <https://doi.org/10.1155/2021/1884293>.
- [31] P. Patnaik, *Handbook of inorganic chemicals*, McGraw-Hill, New York, 2003.
- [32] V.A. Pustovarov, T.V. Perevalov, V.A. Gritsenko, T.P. Smirnova, A.P. Yelissev, Oxygen vacancy in Al₂O₃: Photoluminescence study and first-principle simulation, *Thin Solid Films.* 519 (2011) 6319–6322. <https://doi.org/10.1016/j.tsf.2011.04.014>.
- [33] B.A. Sperling, B. Kalanyan, J.E. Maslar, Atomic Layer Deposition of Al₂O₃ Using Trimethylaluminum and H₂O: The Kinetics of the H₂O Half-Cycle, *J. Phys. Chem. C.* 124 (2020) 3410–3420. <https://doi.org/10.1021/acs.jpcc.9b11291>.
- [34] S. Vlassov, B. Polyakov, M. Vahtrus, M. Mets, M. Antsov, S. Oras, A. Tarre, T. Arroval, R. Löhmus, J. Aarik, Enhanced flexibility and electron-beam-controlled shape recovery in alumina-coated Au and Ag core–shell nanowires, *Nanotechnology.* 28 (2017) 505707. <https://doi.org/10.1088/1361-6528/aa973c>.
- [35] B. Polyakov, R. Zabels, A. Sarakovskis, S. Vlassov, A. Kuzmin, Plasmonic photoluminescence enhancement by silver nanowires, *Phys. Scr.* 90 (2015) 094008. <https://doi.org/10.1088/0031-8949/90/9/094008>.
- [36] A. Kuzmin, R. Kalendarev, A. Kursitis, J. Purans, Confocal spectromicroscopy of amorphous and nanocrystalline tungsten oxide films, *J. Non-Cryst. Solids.* 353 (2007) 1840–1843. <https://doi.org/10.1016/j.jnoncrysol.2007.02.014>.
- [37] S.K. Panda, A. Dev, S. Chaudhuri, Fabrication and Luminescent Properties of c-Axis Oriented ZnO–ZnS Core–Shell and ZnS Nanorod Arrays by Sulfidation of Aligned ZnO Nanorod Arrays, *J. Phys. Chem. C.* 111 (2007) 5039–5043. <https://doi.org/10.1021/jp068391c>.
- [38] X. Li, X. Li, B. Zhu, J. Wang, H. Lan, X. Chen, Synthesis of porous ZnS, ZnO and ZnS/ZnO nanosheets and their photocatalytic properties, *RSC Adv.* 7 (2017) 30956–30962. <https://doi.org/10.1039/C7RA03243A>.
- [39] L. Yu, W. Chen, D. Li, J. Wang, Y. Shao, M. He, P. Wang, X. Zheng, Inhibition of photocorrosion and photoactivity enhancement for ZnO via specific hollow ZnO core/ZnS shell structure, *Appl. Catal. B Environ.* 164 (2015) 453–461. <https://doi.org/10.1016/j.apcatb.2014.09.055>.
- [40] H. Ci, L. Ma, X. Liu, Y. Liang, Y. Zheng, Z. Li, S. Zhu, Z. Cui, S. Wu, Photo-excited antibacterial poly(ϵ -caprolactone)@MoS₂/ZnS hybrid nanofibers, *Chem. Eng. J.* 434 (2022) 134764. <https://doi.org/10.1016/j.cej.2022.134764>.
- [41] Y.-H. Lee, X.-Q. Zhang, W. Zhang, M.-T. Chang, C.-T. Lin, K.-D. Chang, Y.-C. Yu, J.T.-W. Wang, C.-S. Chang, L.-J. Li, T.-W. Lin, Synthesis of Large-Area MoS₂ Atomic Layers with Chemical Vapor Deposition, *Adv. Mater.* 24 (2012) 2320–2325. <https://doi.org/10.1002/adma.201104798>.
- [42] A.L. Elías, N. Perea-López, A. Castro-Beltrán, A. Berkdemir, R. Lv, S. Feng, A.D. Long, T. Hayashi, Y.A. Kim, M. Endo, H.R. Gutiérrez, N.R. Pradhan, L. Balicas, T.E. Mallouk, F. López-Urías, H. Terrones, M. Terrones, Controlled Synthesis and Transfer of Large-Area WS₂ Sheets: From Single Layer to Few Layers, *ACS Nano.* 7 (2013) 5235–5242. <https://doi.org/10.1021/nn400971k>.
- [43] P. Tonndorf, R. Schmidt, P. Böttger, X. Zhang, J. Börner, A. Liebig, M. Albrecht, C. Kloc, O. Gordan, D.R.T. Zahn, S.M. de Vasconcellos, R. Bratschitsch, Photoluminescence

- emission and Raman response of monolayer MoS₂, MoSe₂, and WSe₂, *Opt. Express*. 21 (2013) 4908–4916. <https://doi.org/10.1364/OE.21.004908>.
- [44] J.H. Parker, D.W. Feldman, M. Ashkin, Raman Scattering by Silicon and Germanium, *Phys. Rev.* 155 (1967) 712–714. <https://doi.org/10.1103/PhysRev.155.712>.
- [45] K.A. Alim, V.A. Fonoberov, M. Shamsa, A.A. Balandin, Micro-Raman investigation of optical phonons in ZnO nanocrystals, *J. Appl. Phys.* 97 (2005) 124313. <https://doi.org/10.1063/1.1944222>.
- [46] Y.C. Cheng, C.Q. Jin, F. Gao, X.L. Wu, W. Zhong, S.H. Li, P.K. Chu, Raman scattering study of zinc blende and wurtzite ZnS, *J. Appl. Phys.* 106 (2009) 123505. <https://doi.org/10.1063/1.3270401>.
- [47] S.P.S. Porto, R.S. Krishnan, Raman Effect of Corundum, *J. Chem. Phys.* 47 (1967) 1009–1012. <https://doi.org/10.1063/1.1711980>.
- [48] S.M. Prokes, M.B. Katz, M.E. Twigg, Growth of crystalline Al₂O₃ via thermal atomic layer deposition: Nanomaterial phase stabilization, *APL Mater.* 2 (2014) 032105. <https://doi.org/10.1063/1.4868300>.
- [49] C.-S. Ku, H.-Y. Lee, J.-M. Huang, C.-M. Lin, Epitaxial Growth of *m*-Plane ZnO Thin Films on (10 $\bar{1}$ 0) Sapphire Substrate by Atomic Layer Deposition with Interrupted Flow, *Cryst. Growth Des.* 10 (2010) 1460–1463. <https://doi.org/10.1021/cg9013043>.
- [50] F.L. Deepak, A. Mayoral, A.J. Steveson, S. Mejía-Rosales, D.A. Blom, M. José-Yacamán, Insights into the capping and structure of MoS₂ nanotubes as revealed by aberration-corrected STEM, *Nanoscale*. 2 (2010) 2286. <https://doi.org/10.1039/c0nr00484g>.
- [51] L. Peters, C. Ó Coileáin, P. Dluzynski, R. Siris, G.S. Duesberg, N. McEvoy, Directing the Morphology of Chemical Vapor Deposition-Grown MoS₂ on Sapphire by Crystal Plane Selection, *Phys. Status Solidi A*. 217 (2020) 2000073. <https://doi.org/10.1002/pssa.202000073>.
- [52] Z. Ma, S. Wang, Q. Deng, Z. Hou, X. Zhou, X. Li, F. Cui, H. Si, T. Zhai, H. Xu, Epitaxial Growth of Rectangle Shape MoS₂ with Highly Aligned Orientation on Twofold Symmetry *a*-Plane Sapphire, *Small*. 16 (2020) 2000596. <https://doi.org/10.1002/sml.202000596>.
- [53] H. Bergeron, V.K. Sangwan, J.J. McMorrow, G.P. Campbell, I. Balla, X. Liu, M.J. Bedzyk, T.J. Marks, M.C. Hersam, Chemical vapor deposition of monolayer MoS₂ directly on ultrathin Al₂O₃ for low-power electronics, *Appl. Phys. Lett.* 110 (2017) 053101. <https://doi.org/10.1063/1.4975064>.
- [54] Ø.S. Fjellvåg, A. Ruud, H.H. Sønsteby, O. Nilsen, H. Fjellvåg, Crystallization, Phase Stability, and Electrochemical Performance of β -MoO₃ Thin Films, *Cryst. Growth Des.* 20 (2020) 3861–3866. <https://doi.org/10.1021/acs.cgd.0c00156>.
- [55] H. Qin, P. Sutter, G. Zhou, The Crystallization of Amorphous Aluminum Oxide Thin Films Grown on NiAl(100), *J. Am. Ceram. Soc.* 97 (2014) 2762–2769. <https://doi.org/10.1111/jace.13036>.
- [56] H.Y. Wang, C.R. Wang, J. Xu, X. Liu, X.F. Xu, H.Z. Xing, L.J. Zhao, X.S. Chen, Different temperature dependence of excitonic and defect-related photoluminescence spectra in ZnS nanobelts and nanowires, *J. Phys. Appl. Phys.* 45 (2012) 095301. <https://doi.org/10.1088/0022-3727/45/9/095301>.
- [57] H. Chen, Y. Hu, X. Zeng, Green photoluminescence mechanism in ZnS nanostructures, *J. Mater. Sci.* 46 (2011) 2715–2719. <https://doi.org/10.1007/s10853-010-5141-9>.
- [58] I. Shalish, H. Temkin, V. Narayanamurti, Size-dependent surface luminescence in ZnO nanowires, *Phys. Rev. B*. 69 (2004) 245401. <https://doi.org/10.1103/PhysRevB.69.245401>.